

Towards quantitative precision in the chiral crossover: masses and fluctuation scales

Alexander J. Helmboldt,¹ Jan M. Pawłowski,^{1,2} and Nils Strodthoff¹

¹*Institut für Theoretische Physik, Universität Heidelberg, Philosophenweg 16, 69120 Heidelberg, Germany*

²*ExtreMe Matter Institute EMMI, GSI, Planckstr. 1, 64291 Darmstadt, Germany*

We investigate the relation between the physical pion pole and screening masses and the mesonic fluctuation scale in low-energy QCD, which relates to the curvature of the mesonic effective potential. This relation is important for the correct relative weight of quantum, thermal and density fluctuations. Hence, it governs the location of phase boundaries as well as the phase structure of QCD. The identification of the correct physics scales is also primarily important for the correct adjustment of the parameters of effective models for low-energy QCD. It is shown that subject to an appropriate definition of the latter, all these scales agree at vanishing temperature, while they deviate from each other at finite temperature.

PACS numbers: 12.38.Aw, 11.10.Wx, 11.30.Rd, 12.38.Gc

I. INTRODUCTION

In the past decade rapid progress has been made in our theoretical understanding of the QCD phase structure, both with continuum methods and with the lattice. By now, functional continuum approaches to QCD allow us to discuss the strongly correlated low-energy sector within a first-principle approach. Then the couplings to be fixed are simply the fundamental parameters of QCD: the strong coupling α_s and the current quark masses m_{current} , see [1–4]. In principle, this approach also allows to pin down the coupling constants in low-energy effective models of QCD as functions of α_s and m_{current} . These models are usually defined at a (UV) momentum scale Λ_{UV} of about 1 GeV in terms of an effective Lagrangian with a set of coupling parameters $\bar{\lambda}$. As low-energy couplings of QCD they can be deduced uniquely from QCD as $\bar{\lambda}(\alpha_s, m_{\text{current}})$. Such an approach is completed by determining the set of all relevant low-energy coupling parameters (at the UV scale Λ_{UV}) which may have an impact on the infrared physics at hand. In summary, this set-up anchors low-energy models within first-principle QCD and their independent couplings are only those of QCD. As a consequence, not only qualitative but also quantitative physics questions of the strongly correlated low-energy sector of QCD become accessible.

As described above, it is of chief importance in this set-up to pin down the relevant couplings in low-energy models. Moreover, the analysis of low-energy quantum, thermal and density fluctuations in these models have to be brought to a quantitative level. The current work does a further significant step in this direction in the context of the quark-meson (QM) model. We study the frequency and momentum dependence of two-point correlation functions, which is interesting for several reasons. Most importantly, it gives us direct access to the relevant question of physical observables such as pole masses and decay constants, which are so far only indirectly accessible in the Euclidean approach. Within this context it also allows us to determine and clarify the relations between the physical observables determined at the poles,

e.g. at $p^2 = -m_\pi^2$ and the low-energy parameters of the models at $p^2 = 0$. In particular, we determine the relations between pole masses corresponding to propagator poles at $p_0^2 = -m_{\text{pol}}^2$, screening masses corresponding to poles at $\vec{p}^2 = -m_{\text{scr}}^2$ and curvature masses m_{cur}^2 evaluated at $p^2 = 0$. Only the latter are directly accessible within Euclidean approaches and are the mass parameters in the effective action.

So far, the above relation and its convergence with a given approximation scheme has not been studied. However, this is chiefly important for the relative weight of quantum, thermal and density fluctuations: The characteristic scale of quantum fluctuations is the curvature mass m_{cur} . Below this mass scale the propagation of quantum fluctuations is suppressed. In turn, the characteristic scale of density fluctuations is the pole mass m_{pol} (of modes with non-vanishing quark number). At finite temperature these scales have some temperature dependence. Thus, the correct identification of m_{pol} , m_{scr} and m_{cur} is an important issue in particular for quantitative approaches towards QCD at finite temperature and density, where potential mismatches can lead to large systematic errors.

We discuss this issue at the example of the derivative expansion, which is an expansion in momenta over mass-scale, p^2/m^2 . The derivative expansion is the most popular expansion scheme used in low-energy effective models. In most applications the local potential approximation (LPA) is used, where one employs classical propagators. In contrast, the computation in the present work involves fully momentum-dependent propagators. This advanced approximation can be used to resolve apparent inconsistencies reported in the literature within the LPA, see [5–7]. Finally, we also evaluate the quality of the LPA' scheme, which includes momentum-independent wavefunction renormalisation factors, in comparison to the full calculation.

The strength of our computational approach lies in the fact, that it provides a stable numerical iteration procedure with only little numerical overhead compared to the momentum-independent calculation. From the technical

point of view, the method is applicable to a wide range of possible theories. Furthermore, it can be extended to complex external momenta along the lines of [5, 6, 8–10] hence providing direct access to spectral functions in an Euclidean framework without the need for analytical continuation of given Euclidean data.

The article is organised as follows. In Sect. II we discuss the embedding of low-energy effective models, and specify the effective action of the quark-meson model. We also elaborate on the different mass definitions and their physics content, as well as providing a brief introduction to the functional renormalisation group (FRG) and the computational set-up. In Sect. III we present the results of mass calculations at vanishing and finite temperature. We discuss the implications for relative fluctuation scales in particular in view of the chiral phase boundary. Furthermore, we compare LPA, LPA' and the calculation with fully momentum-dependent mesonic propagators in terms of quantitative accuracy. The latter is henceforth referred to as full calculation.

II. LOW-ENERGY QCD AND FLUCTUATIONS

A. Low-energy effective models

We aim at describing the low-energy sector of two-flavor QCD within a quark-meson model [11–14]. As already mentioned in the introduction, low-energy effective models can be firmly anchored in first-principle QCD, see [1–4]. The key idea behind this embedding in full QCD is the functional RG approach to QCD with dynamical hadronisation, [15–18]. There, the flow is initiated at a large momentum scale $\Lambda_{\text{UV}} \gg \Lambda_{\text{QCD}}$, where it starts with the effective action of perturbative QCD with dynamical quarks and gluons. Then, by lowering the momentum scale within this first-principle QCD framework, the hadronic degrees of freedom get dynamical at the hadronisation scale, while the quark and gluon degrees of freedom decouple. This is most simply seen in the Landau gauge, where the gluon propagator is infrared gapped, the gapping being directly related to the QCD mass gap, see e.g. [19]. Accordingly, the gluons can be integrated out first, leading to an effective theory with quarks and hadronic degrees of freedom in a gluonic background potential at a momentum scale $\Lambda_{\text{UV}} \approx 1 \text{ GeV}$, such as Polyakov loop enhanced low-energy models. First results within such a QCD-enhanced model approach have been presented in [3, 4]. This setting entails, that first-principle QCD flows can be employed to provide initial parameters and further glue input, such as background potentials, for model calculations, thereby systematically removing ambiguities in these approaches.

The QCD computation relies only on two input parameters, the strong coupling α_s and the current quark mass m_{current} , and allows to consistently include quantum and thermal fluctuations, where hadronic correlations are captured via the dynamical hadronisation. In

this way model computations can profit directly from a systematic improvement in predictive power. Conversely, the quantitative advances in model calculations, such as put forward in this work, can be easily carried over to full QCD computation. This allows to systematically improve the approximation of the first-principle QCD flows in the low-energy regime.

In this work we study a quark-meson model taking into account the momentum dependence of mesonic two-point functions. At vanishing temperature, the model in the presence of low-energy quantum fluctuations is approximated by an effective action of the form

$$\Gamma = \int_x \left\{ \bar{\psi} (\not{D} + h(\sigma + i\gamma^5 \vec{\tau} \cdot \vec{\pi})) \psi + \frac{1}{2} Z \partial_\mu \phi_i \partial_\mu \phi_i + \frac{1}{8} Y \partial_\mu \rho \partial_\mu \rho + U(\rho) \right\}. \quad (1)$$

Here $\rho = \sigma^2 + \vec{\pi}^2$, and we include momentum- and field-dependent bosonic wavefunction renormalisation factors $Z = Z(p^2; \rho)$ and $Y = Y(p^2; \rho)$. The bosonic sector corresponds to a fluctuating $O(N)$ model [20, 21], while the fermionic sector is classical, anticipating the decoupling of quark fluctuations at low energies and temperatures. In the following, we expand Z and Y about a field value ρ_0 , restricting ourselves to the zeroth order terms, i.e. $Z = Z(p^2; \rho_0)$ and $Y = Y(p^2; \rho_0)$. However, we take into account the full momentum dependence of Z, Y , as well as computing a full effective potential $U(\rho)$. The quantitative accuracy of a low order in the field-expansion of Z has been tested in [22], which is in this work extended by the inclusion of Y . The mesonic two-point functions, evaluated at a constant field configuration $\phi_i = (\sqrt{\rho}, \vec{0})_i$, read

$$\begin{aligned} \Gamma_{\pi_i \pi_j}^{(2)} &= \delta_{ij} Z_\pi p^2 + 2U'(\rho) \delta_{ij}, \\ \Gamma_{\sigma\sigma}^{(2)} &= Z_\sigma p^2 + 2U'(\rho) + 4U''(\rho) \rho, \end{aligned} \quad (2)$$

where $Z_\pi = Z(p^2; \rho_0)$ and $Z_\sigma = Z(p^2; \rho_0) + Y(p^2; \rho_0) \rho$.

B. Pole-, screening- and curvature masses

Particle masses can be extracted directly from the fully momentum-dependent propagators. In this section, we review different mass definitions based on the renormalised inverse two-point function $\bar{\Gamma}^{(2)}(p_0, \vec{p}^2) = \Gamma^{(2)}(p_0, \vec{p}^2) / \bar{Z}$. Here, the momentum-independent wavefunction renormalisation \bar{Z} relates the bare field ϕ to the renormalised field

$$\bar{\phi} = \bar{Z}^{\frac{1}{2}} \phi. \quad (3)$$

At vanishing temperature the wavefunction renormalisation \bar{Z} is directly related to $Z = Z_\pi$ in (1) evaluated at some fixed external momentum. In turn, at finite temperature the heat bath singles out a rest frame, and the wave function renormalisation Z splits into one compo-

nent parallel, Z_{\parallel} , and one perpendicular, Z_{\perp} , to the heat bath. Accordingly, we parameterise the inverse propagator (at $\rho = \rho_0$) as

$$\Gamma^{(2)}(p_0, \vec{p}^2) = Z_{\parallel}(p_0, \vec{p}^2)p_0^2 + Z_{\perp}(p_0, \vec{p}^2)\vec{p}^2 + m^2, \quad (4)$$

with Z_{\parallel}, Z_{\perp} being finite for vanishing momentum and/or frequency. While the decomposition in (4) into $Z_{\parallel}(p_0, \vec{p}^2)$ and $Z_{\perp}(p_0, \vec{p}^2)$ is not unique for general momenta, it is for vanishing $|\vec{p}|$ or p_0 . Hence, we can define momentum-independent wavefunction renormalisation factors parallel and perpendicular to the heat bath within an evaluation at $p_0 = 0$ or $\vec{p} = 0$, respectively, i.e.

$$\begin{aligned} Z_{\parallel} &= \lim_{p_0 \rightarrow 0} \frac{\Delta\Gamma^{(2)}(p_0, 0)}{p_0^2}, \\ Z_{\perp} &= \lim_{|\vec{p}| \rightarrow 0} \frac{\Delta\Gamma^{(2)}(0, \vec{p}^2)}{\vec{p}^2}, \end{aligned} \quad (5)$$

where $\Delta\Gamma^{(2)}(p_0, \vec{p}^2) \equiv \Gamma^{(2)}(p_0, \vec{p}^2) - \Gamma^{(2)}(0, 0)$. Then a standard choice at finite temperature for the renormalisation of the field is $\bar{Z} = Z_{\perp}$. This definition interpolates between the $O(4)$ -symmetric definition at $T = 0$ with $\bar{Z} = Z_{\perp} = Z_{\parallel}$ to that of the dimensionally reduced theory for $T \rightarrow \infty$, where the propagation is perpendicular to the heat bath. This choice is based on the mass scale of spatial quantum fluctuations. The ratio Z_{\parallel}/Z_{\perp} gives the relative weight of the temporal and spatial fluctuations, and hence is susceptible to the difference of the scale of thermal and quantum fluctuations.

Now we define pole (m_{pol}), screening (m_{scr}), and curvature (m_{cur}) masses via

$$\begin{aligned} \bar{\Gamma}^{(2)}(im_{\text{pol}}, 0) &= 0, \\ \bar{\Gamma}^{(2)}(0, |\vec{p}|^2 = -m_{\text{scr}}^2) &= 0, \\ \bar{\Gamma}^{(2)}(0, 0) &= m_{\text{cur}}^2, \end{aligned} \quad (6)$$

assuming propagator poles at real p^2 . The masses $m_{\text{pol}}^2, m_{\text{scr}}^2$ are the solutions to (6) with the minimal distance to $p^2 = 0$, in general they have a minimal distance to the Euclidean frequency axis. Accordingly, the pole and screening masses are respective inverse temporal and spatial screening lengths. For minimal distance poles at $\pm im_{\text{pol}}$ and $\pm im_{\text{scr}}$, we find an exponential decay of the propagator in position space,

$$\begin{aligned} T \sum_{p_0} [\Gamma^{(2)}(p_0, 0)]^{-1} e^{ip_0 t} &\sim e^{-m_{\text{pol}}|t|}, \\ \int d^3p [\Gamma^{(2)}(0, \vec{p}^2)]^{-1} e^{i\vec{p} \cdot \vec{x}} &\sim e^{-m_{\text{scr}}|\vec{x}|}, \end{aligned} \quad (7)$$

for $|t| \rightarrow \infty$ and $|\vec{x}| \rightarrow \infty$, respectively. At vanishing temperature $\Gamma^{(2)}$ is a function of the $O(4)$ invariant $p_0^2 + \vec{p}^2$

and hence pole and screening masses agree by definition, i.e. $m_{\text{pol}} = m_{\text{scr}}$. At finite temperatures, the ratio of pole and screening masses is given by

$$\frac{m_{\text{pol}}^2}{m_{\text{scr}}^2} = \frac{Z_{\perp}(0, \vec{p}^2 = -m_{\text{scr}}^2)}{Z_{\parallel}(im_{\text{pol}}, 0)}. \quad (8)$$

Due to the breaking of Euclidean $O(4)$ -invariance via the heat bath, the ratio (8) takes values different from unity. In general it is also different from $Z_{\parallel}/Z_{\perp} = Z_{\parallel}(0, \vec{0})/Z_{\perp}(0, \vec{0})$ which is accessible in finite-temperature LPA' calculations, e.g. [23]. Naturally pole and screening masses take different values at finite temperature. Moreover, these differences due to the breaking of Euclidean $O(4)$ -invariance extend to the momentum and frequency dependence and to finite chemical potential.

Note that contrary to pole and screening masses, which are directly physics observables, the curvature mass is not. This is already obvious from the fact that it depends on the renormalisation prescription. For $\bar{Z} = Z_{\perp}$ it relates to the screening mass, but is not identical with the latter. A more detailed discussion is presented below in the context of the finite temperature case.

Finally, in the vacuum in relativistic theories one also has the onset mass m_{ons} . Its definition exploits the fact that the critical chemical potential associated to the onset of a condensation phenomenon is linked to the pole mass m_{pol} of the lightest resonance with non-vanishing quark or baryon number via an exact Silver Blaze argument [24]. The onset mass m_{ons} coincides with the lightest pole mass in the quark propagator by a Silver Blaze argument, which can be shown in any diagrammatic expansion scheme in full propagators such as the functional renormalisation group approach or a 2PI-expansion. The chemical potential enters the propagator as an imaginary shift of the zero momentum component. Hence, there is no dependence of the frequency integrals on the chemical potential until the chemical potentials exceeds the closest singularity to the real (Euclidean) p_0 -axis of the quark propagator in the complex p_0 -plane. The position of this singularity coincides with the pole mass of the corresponding resonance. This agreement between pole and onset mass was checked explicitly in [5] in a numerical calculation within the LPA. We emphasise that in such a diagrammatic approach diagrams contributing to the meson propagators or higher correlation functions with vanishing quark number are not directly sensitive to the chemical potential up to the onset mass in the quark propagator.

It remains to establish a connection between pole and curvature mass. With our choice $\bar{Z} = Z_{\perp}$ we find

$$m_{\text{cur}}^2 = \frac{Z_{\parallel}(im_{\text{pol}}, 0)}{\bar{Z}} m_{\text{pol}}^2 = \frac{Z_{\parallel}(im_{\text{pol}}, 0)}{Z_{\perp}(0, 0)} m_{\text{pol}}^2. \quad (9)$$

In particular, at zero temperature the ratio $m_{\text{cur}}^2/m_{\text{pol}}^2$ is given by the ratio $Z(-m_{\text{pol}}^2)/Z(0)$. This entails that pole and curvature masses still agree approximately at

vanishing temperature if the momentum dependence of $Z(p^2)$ is rather mild for $|p^2| < m_{\text{pol}}^2$. Assuming a well-behaved analytic continuation for these momenta this is tightly linked to a mild momentum dependence of $Z(p^2)$ on Euclidean momenta $p^2 \geq 0$.

We emphasise again that the curvature mass is not defined uniquely. In particular, we may define $\bar{Z} = Z_{\parallel}(im_{\text{pol}}, 0)$, for which both definitions agree. This is to be expected from the Källén-Lehmann spectral representation which relies on expanding about the particle pole.

At zero temperature the equality $m_{\text{pol}} = m_{\text{cur}}$ is best achieved by parameterising the inverse propagator as $\Gamma^{(2)}(p^2) = Z(p^2)(p^2 + m_{\text{pol}}^2)$ and by renormalising the fields with $Z(p^2 = 0)$. For computational convenience, we choose $\bar{Z} = Z_1$ with (4), (5). Then the equality is not guaranteed and hence all statements about the approximate equality of these masses should be understood as statements about the mild momentum dependence of the wavefunction renormalisation. As a final remark, in truncation schemes with momentum-independent wavefunction renormalisation factors, such as LPA or LPA', pole and curvature mass naturally agree if one chooses to renormalise with $\bar{Z} = Z$.

C. Flow equations and momentum dependence

For the computation of the effective potential $U(\rho)$ and the momentum- and frequency-dependent two-point functions $\Gamma^{(2)}(p_0, \vec{p}^2)$ we use the functional renormalisation group, for QCD-related reviews see [17, 21, 25–27]. It is based on the Wilsonian idea of integrating fluctuations momentum shell by momentum shell. Technically this is achieved by introducing an IR regulator function R_k which suppresses quantum fluctuations from momentum modes with momenta smaller than some RG scale k which is subsequently taken from some large UV scale to zero. The evolution of the scale-dependent analogue of the effective action Γ , the effective average action Γ_k , is described by a simple 1-loop equation involving full field-dependent propagators [28],

$$\partial_t \Gamma_k[\psi, \phi] = \frac{1}{2} \text{Tr} \frac{1}{\Gamma_k^{(2)}[\psi, \phi] + R_k} \partial_t R_k, \quad (10)$$

where $\Gamma_k^{(2)}$ denotes the second functional derivative of Γ_k with respect to the fields and $t = \log k/\Lambda$ with some reference scale Λ . The trace Tr sums over momenta and frequencies, internal indices as well as over field species including the standard relative minus sign for the fermionic loop. The corresponding functional equations can rarely be solved exactly. For the present task we resort to the ansatz (1), which includes momentum- and frequency-dependent wavefunction renormalisation factors Z_k and Y_k as well as a full effective potential U_k . Approximations with full momentum and frequency dependence have been applied since long within the FRG, see e.g.

FIG. 1. Flow of the momentum-dependent part of the two-point function $\Delta\Gamma^{(2)}$. Dashed (solid) lines denote full mesonic (quark) propagators and crossed circles correspond to insertions of $\partial_t R_k$ of the respective fields. Tadpole contributions cancel in the present truncation with momentum-independent mesonic vertices.

[19, 29–33], applications in higher orders of the derivative expansions are found in e.g. [34, 35]. In the present work we suggest a new iterative procedure for the solution of fully momentum- and field-dependent approximations with relatively small numerical costs.

Furthermore, although we do not include a genuine running of the Yukawa coupling as in [22], one either computes at a fixed bare or renormalised Yukawa coupling. However, in full QCD flows the renormalised Yukawa coupling stays approximately constant [36]. Hence we employ the latter choice, further details can be found in App. F. The expressions for the inverse propagators, see (4), generalise at finite k similarly to the effective potential. The flow equations for the inverse two-point functions can be obtained from (10) by taking two functional derivatives and are represented diagrammatically in Fig. 1. In general, these flow equations involve three- and four-point vertices as input, which are in our case computed from the effective potential, see App. A for details on the truncation scheme. In our truncation the flow equation for the effective potential takes the schematic form

$$\partial_t U_k(\rho) = \mathcal{F}_U[U_k, \Delta\Gamma_k^{(2)}](\rho) \quad (11)$$

where $\Delta\Gamma_k^{(2)}(q^2) = \Gamma_k^{(2)}(q^2) - \Gamma_k^{(2)}(0)$ at $\rho = \rho_0$. Its flow is given by

$$\partial_t \Delta\Gamma_k^{(2)}(p^2) = \mathcal{F}_G[U_k, \Delta\Gamma_k^{(2)}](\rho_0, p^2). \quad (12)$$

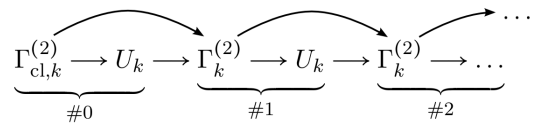


FIG. 2. Illustration of the iteration procedure.

The explicit form of the flow equations is specified in App. A. In the following, we expand (11) about a field value ρ_0 . Then (11) and (12) constitute an equation system which can be solved by an iterative procedure, which is illustrated pictorially in Fig. 2 and described in App. B. In general, this iterative method enjoys very good convergence properties. Concerning the expansion in powers of the field, it has been shown in [22] that an expansion about a fixed bare field has the best convergence properties. For further details we refer the reader to App. F.

III. RESULTS

In the present section we discuss results within the converged iterative method introduced above. The approach put forward in the previous section allows us to discuss the relation between the different fluctuation scales present in the mesonic sector of QCD: despite its non-uniqueness the curvature mass relates to the fluctuation scale of quantum fluctuations. The ratios of Z_\perp/Z_\parallel , and $m_{\text{cur}}/m_{\text{scr}}$, are a measure for the relative strength of thermal fluctuations while the pole mass is the fluctuation scale of density fluctuations.

Additionally, we are interested in the question after the simplest approximation that already includes all quantitative effects.

A. Masses and fluctuation scales

At zero temperature, it is sufficient to numerically investigate the relative size of pole and curvature mass. Screening and pole mass are equal due to Euclidean $O(4)$ invariance. This holds true for all cutoff scales and iteration steps, as the regulators used here preserve $O(4)$ symmetry. As a first non-trivial finding we obtain rather similar pole and curvature masses, with relative deviations of less than one percent, see Tabs. I-III for calculations at different UV cutoff scales. This result is tightly linked to a mild momentum dependence of the wavefunction renormalisation, see the discussion after (9).

step	m_{cur} [MeV]	m_{pol} [MeV]	σ_{min} [MeV]
0	198.1	198.1	58.2
1	135.2	133 ± 2	92.5
2	135.3	133 ± 2	92.8
3	135.3	133 ± 2	92.9
4	135.3	133 ± 2	92.8
5	135.3	133 ± 2	92.9

TABLE I. Pion curvature and pole masses and the minimum of the effective potential for different iteration steps at $T = 0$ for a physical parameter set at $\Lambda_{\text{UV}} = 500$ MeV. The UV parameters are tuned such that the physical pion mass emerges as the fully converged result. Using the same parameters for a LPA' calculation one obtains $m_{\text{pol}} = m_{\text{cur}} = 135.0$ MeV.

step	m_{cur} [MeV]	m_{pol} [MeV]	σ_{min} [MeV]
0	412.8	412.8	16.8
1	144.8	142 ± 2	83.5
2	136.4	135 ± 2	91.8
3	135.1	134 ± 2	93.1
4	134.9	133 ± 2	93.2
5	134.9	133 ± 2	93.2

TABLE II. Similar to Tab. I but for $\Lambda_{\text{UV}} = 700$ MeV. LPA' masses: 135.2 MeV.

step	m_{cur} [MeV]	m_{pol} [MeV]	σ_{min} [MeV]
0	817.0	817.0	5.1
1	163.4	158 ± 2	67.9
2	138.5	137 ± 2	89.9
3	136.5	135 ± 2	92.4
4	135.4	134 ± 2	93.6
5	135.3	134 ± 2	93.6

TABLE III. Similar to Tab. I but for $\Lambda_{\text{UV}} = 900$ MeV. LPA' masses: 134.1 MeV.

The larger the UV cutoff, the more difficult the iteration procedure gets from the numerical point of view and the slower the convergence within the iteration procedure gets. This is illustrated in Tab. I and Tab. III, where the calculation at the smaller cutoff scale converges practically after the first iteration step, whereas the calculation at the larger cutoff scale requires more than three iteration steps until approximate convergence is reached. The reason for the slower convergence has to be found in the fixed renormalised Yukawa coupling as a calculation with a fixed bare Yukawa coupling, irrespective of the chosen UV cutoff scale, shows similarly good convergence properties as our calculation at the lowest cutoff scale, see App. F. In a calculation with a fixed renormalised coupling, as employed here, the fermionic contribution, as the dominant contribution to the flow at large cutoff scales, is no longer decoupled from the bosonic parts of the model but dependent on the wavefunction renormalisation Z . In particular, there is a relevant running of Z at large cutoff scales, which makes the calculation increasingly difficult from the numerical point of view with increasing cutoff scales. However, the most important conclusion from this section remains the approximate agreement of pole and curvature masses at vanishing temperature in the fully iterated result.

At finite temperature, pole and screening masses start to deviate as expected from (8), see Fig. 3 for the pion masses. For a similar observation in the NJL model see e.g. [37]. All low-energy effective models have in common that they have a *physical* UV scale above which they lose predictive power. In the present formulation this scale is given by the initial cutoff scale Λ_{UV} . The thermal range Λ_T of the model is defined as the minimal cutoff scale Λ_{UV} above which thermal fluctuations do not probe the

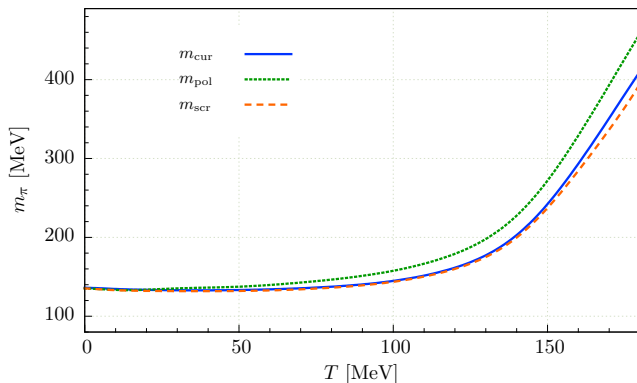


FIG. 3. Temperature dependence of different pion mass definitions extracted from fully iterated result at $\Lambda_{UV} = 1.4$ GeV.

cutoff scale. This is investigated in App. C and leads to $\Lambda_T \lesssim 7T$ for the regulators used, see (A2) with $m = 2$.

Here we present results for temperatures $T \lesssim 180$ MeV which is well covered by $\Lambda_{UV} = 1.4$ GeV. The fact that the curvature mass stays close to the screening mass at all temperatures is related to the fact that we chose $\bar{Z} = Z_{\perp}$ to renormalise fields and is once again an expression for small non-trivial momentum dependencies.

The approximate agreement of pole and curvature masses demonstrated above is a consequence of the momentum dependence obtained from the converged iteration procedure. In particular, their difference allows to pin down effects of scale mismatches in existing calculations in simple but commonly used truncation schemes such as the LPA. Here we aim at quantifying the systematic error which is inherent in these calculations. For different cutoff scales we follow the usual procedure in the literature and tune initial conditions such that we obtain correct physical observables in the IR. Then we compute the LPA onset mass by calculating the momentum-dependent meson propagator using the given LPA solution, corresponding to the first half of the first iteration step in Fig. 2. The pole mass extracted from this propagator equals, up to approximation effects, the LPA onset mass, which can be probed directly by including a coupling to (isospin) chemical potential, see [5, 6]. This LPA onset mass can now be compared to the LPA curvature mass extracted from the curvature of the effective potential as shown in Tab. IV. Whereas their ratio tends to one for smaller UV scales, it increases with the UV scale and reaches a value of 1.71 for $\Lambda_{UV} = 1.4$ GeV.

Such large deviations are in line with earlier studies [5, 6] where deviations of 30% were observed for a 3d regulator function and a cutoff scale $\Lambda_{UV} = 900$ MeV. In the present work we use 4d exponential regulators, (A2) with $m = 2$. For different regulators the *physical* cutoff scales, $k_{phys}(k)$ do not necessarily agree, for a detailed discussion and applications see [17, 38]. This entails that coinciding physical cutoff scales are obtained for different regulator scales k . A rough estimate for this ratio of cutoff scales is given by the ratio of the (bosonic) flow of

Λ_{UV} [GeV]	m_{cur} [MeV]	m_{ons} [MeV]	m_{cur}/m_{ons}
0.5	135.0	109 ± 2	1.24
0.7	135.2	98 ± 2	1.38
0.9	135.0	90 ± 2	1.50
1.1	135.4	85 ± 2	1.59
1.4	135.3	79 ± 2	1.71

TABLE IV. Comparison of LPA curvature and onset masses for fixed curvature masses in the IR and different UV cutoff scales Λ_{UV} .

the masses. For the standard exponential regulator (A2) with $m = 1$ we find $k_{3d}/k_{4d,m=1} \approx 3/2$, for the exponential regulator (A2) with $m = 2$ we find $k_{3d}/k_{4d,m=2} \approx 5/4$.

In summary this entails that the commonly used UV cutoff scales $\Lambda_{UV,3d} = 700$ MeV and 900 MeV correspond to UV cutoff scales $\Lambda_{UV,4d,m=2} = 560$ MeV and 720 MeV, respectively. For the following numerical examples we will therefore focus on the case of $\Lambda_{UV,4d,m=2} = 700$ MeV.

At first sight, deviations between the curvature and the onset mass might seem irrelevant for studies at a given expansion order such as the commonly employed zeroth order derivative expansion or LPA. However, as already explained in the beginning of this section, the curvature mass and the ratio Z_{\perp}/Z_{\parallel} sets the relevant scales for quantum and thermal fluctuations while the pole/onset mass is that of density fluctuations. In other words, an approximation scheme where these mass scales differ by 38% leads to a significant quantitative change of the ratio of critical temperature T_c over onset chemical potential μ_c . A rough estimate, assuming that the onset chemical potential/ critical temperature measured in the respective mass scales stays constant in the different approximation schemes, provides

$$\left[\frac{\mu_c}{T_c} \right]_{full} / \left[\frac{\mu_c}{T_c} \right]_{LPA} \approx \left[\frac{m_{cur}}{m_{ons}} \right]_{LPA} \approx 1.38, \quad (13)$$

where the subscript *full* refers to the present momentum-dependent approximation.

This mismatch of scales has consequences for the scale setting procedure in LPA. The commonly used procedure is to fix the physical parameters at the initial UV scale $\Lambda_{UV} = 700$ MeV such, that the pion (pole) mass of approximately 135 MeV is the curvature mass $m_{\pi,cur}$, as it agrees with the pole mass in this order of the derivative expansion (classical dispersion). And indeed the full results of the last section justify this identification. As the scale of quantum and thermal fluctuations is identical in this approximation due to $Z_{\perp}/Z_{\parallel} = 1$, and $m_{cur}/m_{scr} = 1$ all these fluctuations are treated self-consistently. In turn, the scale for density fluctuations in LPA is set by the onset mass, see Tab. IV, which is approximately 98 MeV at a UV cutoff scale $\Lambda_{UV} = 700$ MeV. This entails that the strength of density fluctuations is overestimated by 28%. Alternatively, one can identify the pion mass with the onset mass [5, 6]. With hindsight this comes at the expense of having a too large scale for quantum and ther-

mal fluctuations of about 186 MeV instead of 135 MeV, see Tab. IV. In other words, quantum and thermal fluctuations are underestimated by 38 %.

To summarise, there is no way of circumventing a mismatch of fluctuation scales in a truncation scheme with vastly different curvature and onset masses such as the LPA. Its implications for the chiral phase boundary at finite density are discussed in Sec. III C. Apart from the quantitative change of the phase boundary this mismatch may also inflict qualitative changes at large chemical potential $\mu > \mu_c$, for example if the phase structure at nuclear densities and beyond involves competing order effects.

B. Momentum dependence and initial conditions

In order to study the impact of fully momentum-dependent propagators on FRG calculations in low-energy QCD, we compare the temperature dependence of the quark condensate $\langle\sigma\rangle$ in different orders of the truncation scheme. $\langle\sigma\rangle(T)$ is sensitive to a correct relative inclusion of thermal and quantum fluctuations as well as the absolute scale. We compare three different truncations, namely LPA, LPA' and the fully momentum-dependent calculation.

As already discussed in Sec. II A, there are two possibilities to fix the initial conditions. Firstly, one can derive the initial conditions from computing QCD-flows for the model's parameters in the UV. In the following we evaluate the consequences of this set-up by comparing different simpler truncation schemes to the momentum-dependent calculation put forward in this work, which is expected to lie closest to the full QCD flow. Secondly, one can tune the model parameters such that the vacuum physics of QCD is reproduced within the respective model and approximation scheme. In low-energy QCD without inherent approximations these two sets of initial conditions agree. In turn, within approximations, they are different. Hence, we shall consider both approaches in our investigation separately.

1. Fixed microphysics

We first study the effects of including fully momentum-dependent propagators while keeping the UV-physics of the model fixed at $\Lambda_{UV} = 900$ MeV. In such a QCD-embedded approach the input parameters at Λ_{UV} are derived within QCD flows. However, in this work, we employ a parameter set which leads to correct physical observables in the IR for the full calculation to mimic the effect of fixing initial conditions from full QCD. Our findings for the chiral crossover are summarised in Figs. 4.

On the one hand, note that for a cutoff scale of $\Lambda_{UV} = 900$ MeV no comparison to the LPA is possible because the LPA calculation with initial conditions from the full calculation only shows chiral symmetry breaking

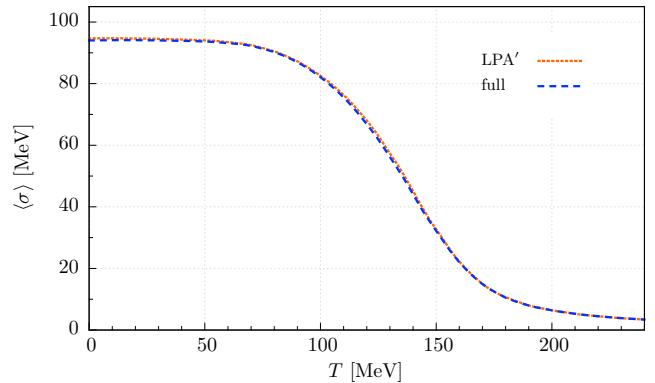


FIG. 4. Chiral condensate vs. temperature for fixed UV parameters using different truncations and $\Lambda_{UV} = 900$ MeV.

for $\Lambda_{UV} < \Lambda_{LPA}^* \approx 600$ MeV, see App. D. Therefore, we restrict ourselves in the LPA case to a comparison at vanishing temperature for a UV cutoff scale $\Lambda_{UV} = 500$ MeV, which can be inferred from Tab. I. Note that with the thermal range $\Lambda_T \lesssim 7T$ we only have access to temperatures $T \lesssim 70$ MeV anyway, see App. C. However, even for $\Lambda_{UV} = 500$ MeV LPA is not quantitatively consistent with the full calculation with deviations of 50 % in $\langle\sigma\rangle$ and m_π .

On the other hand, Fig. 4 shows that the LPA' calculation is even quantitatively consistent with the full result. The largest relative deviations of about 3 % arise in the vicinity of the pseudo-critical temperature T_c and are certainly related to pseudo-critical fluctuations. At about T_c , the correlation length is large, and the system changes its dynamical degrees of freedom from quarks to mesons. Both properties imply that this region is most sensitive to momentum fluctuations. This is also in line with the expectation that including the full momentum dependence or higher orders of the derivative expansion is crucial around the critical temperature T_c , e.g. in order to calculate critical exponents at high numerical precision, see e.g. [35, 39].

The generally very good agreement of LPA' and the fully momentum-dependent truncation in Fig. 4 is intimately related to the use of a cutoff function R_k , which regularises both frequencies p_0 and spatial momenta \vec{p} , see [33, 40]. Thus, the associated RG flows are local both in $|\vec{p}|$ - and in p_0 -space and the argument from the zero temperature discussion in App. G applies. Conversely, if we employed a regulator which only affects spatial momenta, such as is commonly done in finite-temperature FRG calculations, the entire Matsubara summation would be required to compute a given RG flow. Put differently, the flows at every scale k would receive contributions from both very small and very large Matsubara frequencies, thereby at least partly invalidating the $T = 0$ reasoning presented in App. G. Accordingly, calculations based on three-dimensional cutoff functions are anticipated to give rise to deviations which are larger than the ones we observe in Fig. 4.

2. Fixed vacuum physics

In the previous section we have discussed the different truncations in view of the direct connection of the QM model to first-principle QCD. Then the UV initial conditions can in principle, be calculated from QCD flows. Within such a combined approach the QM model can be systematically upgraded to the full low-energy effective action of QCD. This technically challenging programme is well under way, and eventually will give quantitative reliability to enhance low-energy effective model computations.

However, we might also disregard the direct connection to QCD and fix the initial conditions in the infrared by adjusting the correct vacuum physics: choose some generic set of (renormalised) IR observables ($\bar{f}_\pi, \bar{m}_\pi, \bar{m}_\psi$) and then tune the microphysics separately in each truncation scheme such that the given mass scales emerge in the limit $k \rightarrow 0$ at vanishing temperature and density. On the basis of this adjustment one then can study finite-temperature or finite-density physics. This approach is the standard effective model approach to low-energy QCD. The discussion in the present section is meant to evaluate and improve the reliability of this set-up.

Note first that such a procedure falls short of a direct connection to first-principle QCD in the UV. Moreover, in particular in low-order approximations such as LPA, some fluctuation physics is simply stored in the initial condition. For example, in LPA for the model at hand, we have to change the UV initial conditions such that they effectively take care of the missing momentum effects. In order to assess the impact of adding the full momentum dependence on top of a given LPA or LPA' solution, we show in Tab. V the iteration procedure applied to a given LPA or LPA' solution, referred to as zeroth iteration step in Tab. V. On the one hand, as expected from Sec. III A, the iteration on top of the given LPA result shows a large deviation of over 40% in the masses after the first iteration step, illustrating again the large mismatch of fluctuation scales in the LPA. On the other hand, with a deviation of less than one percent, the LPA' solution is already very close to the full re-

step	m_{cur} [MeV]	m_{pol} [MeV]	m_{cur} [MeV]	m_{pol} [MeV]
0	135.2	135.2	135.2	135.2
1	96.5	96 ± 2	135.5	134 ± 2
2	96.8	96 ± 2	135.5	134 ± 2
3	96.8	96 ± 2	135.6	134 ± 2
4	96.8	96 ± 2	135.6	134 ± 2
5	96.8	96 ± 2	135.6	134 ± 2

TABLE V. Pion curvature and pole masses for different iteration steps at $T = 0$ applying the iteration procedure on top of a LPA (left) and a LPA' (right) parameter set for a UV cutoff scale $\Lambda_{\text{UV}} = 700$ MeV. The UV parameters are tuned such that the physical pion mass emerges in the respective zeroth step.

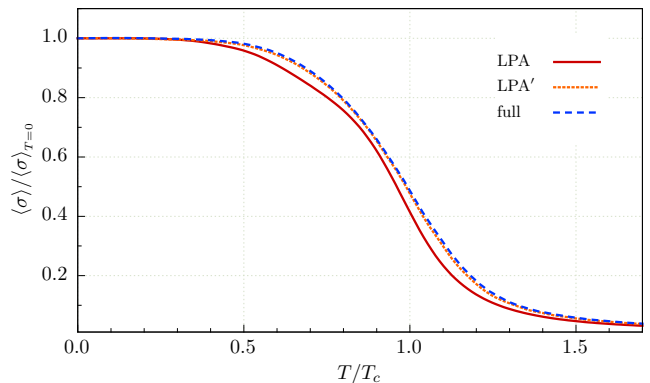


FIG. 5. Chiral condensate vs. temperature for fixed physical IR parameters in the vacuum using different truncations and $\Lambda_{\text{UV}} = 900$ MeV.

sult. Even more conveniently for practical purposes, the first iteration step deviates less than one per mill from the full result. Hence, evaluating the momentum dependence on the basis of a given LPA' solution, already provides a simple but very good approximation to the full momentum-dependent solution.

Our findings on the chiral crossover are summarised in Fig. 5. We again observe that the LPA' scheme approximates the full flow very well. To be more precise, the relative deviation of the chiral condensate never exceeds 3%. Note, however, that the relative deviation again exhibits a peak centered at the pseudo-critical temperature, which indicates accuracy issues in the presence of pseudo-critical fluctuations. Possible reasons for the generally good agreement between the two schemes were already extensively studied in the preceding paragraph as well as in App. G. Accordingly, we will concentrate on the remaining comparison between the LPA and the full calculation.

Here, Fig. 5 reveals that despite large deviations of about 19% in T_c measured in absolute scales, which is to large parts caused by different sigma mass ranges which can be reached in the different approximation schemes, the deviations in terms of relative scales are rather small as well, at least for temperatures outside the critical regime. This presumably reflects the fact, that the propagators' non-trivial momentum dependencies enter the computation of the chiral condensate from the effective potential only indirectly. Put differently, the crossover's shape seems to be mainly fixed by the infrared mass scales in the vacuum.

The quantitative discrepancy between LPA and the full calculation can be understood most easily from Fig. 6, where we compare the scale dependence of the pion mass for fixed initial conditions in the IR as an illustration of cutoff regions where the LPA calculation gives qualitatively or quantitatively correct results compared to the full calculation. Remarkably, both is only the case for cutoff scales below 200 MeV whereas for larger scales the results are not even qualitatively correct as it is clearly

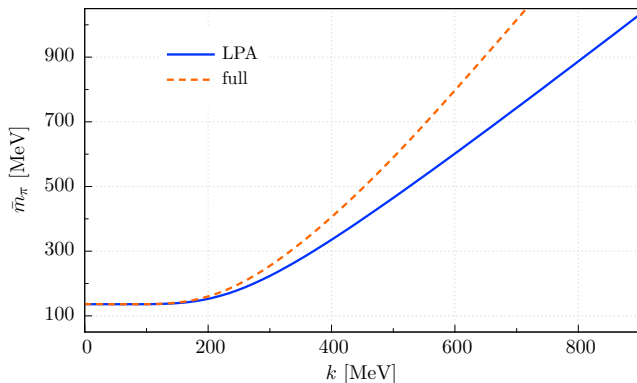


FIG. 6. Scale dependence of the pion mass at $T = 0$ in LPA and in the full calculation for $\Lambda_{UV} = 900$ MeV for fixed physical IR parameters.

visible from the different slopes as a result of the fixed renormalised Yukawa coupling in the full calculation.

C. Finite density

Let us finally evaluate the consequences of the results in the last two sections for finite density computations. These observations point at a mismatch of scales in LPA between quantum/thermal and density fluctuations with a factor as given in Eq. (13). As before we employ the cutoff scale $\Lambda_{UV} = 700$ MeV as numerical example.

To illustrate its consequences we consider a simple application to the physics of the phase diagram in LPA, where we resort to the simple rescaling argument that has worked so successfully for quantum and thermal fluctuations in Section IIIB 2. Within this reasoning, the overestimation of density fluctuations can be approximately undone by simply rescaling the chemical potential axis with a factor 1.38. This weakens the curvature of the chiral phase boundary $T_c(\mu)/T_c(0)$ at finite chemical potential. At small chemical potential the phase boundary can be expanded in powers of μ^2 as follows:

$$\frac{T_c(\mu)}{T_c(0)} = 1 - \kappa_\mu \left(\frac{\mu}{\pi T_c(0)} \right)^2 + \mathcal{O} \left(\left(\frac{\mu}{\pi T_c(0)} \right)^4 \right), \quad (14)$$

for a discussion of the phase structure of the $N_f = 2$ quark-meson model in LPA and LPA' as well as with higher order quark-meson scattering processes see [22]. Eq. (14) entails that a stretching of the chemical potential axis with a factor 1.38 weakens the curvature κ_μ by a factor 0.53. In [22] the curvature was computed from the chiral susceptibility as $\kappa_{\mu, \text{LPA}} \approx 1.4$. Applying the reduction factor, this reduces to $\kappa_\mu \approx 0.74$, which influences the result in the direction of the lattice curvature $\kappa_\mu \approx 0.5$ [41].

The above discussion suggests that taking into account the full momentum dependence of the propagators in the quark-meson model may account for the mismatch be-

tween the curvature of the phase boundary computed in the models and the lattice result. However, [22] also contains a computation with constant wavefunction renormalisations for meson and quark fields (LPA') and a fully (meson-)field-dependent Yukawa coupling (corresponding to higher order quark-mesonic scattering processes). The curvature κ_μ for this computation agrees surprisingly well with the LPA result. This means that either the higher order quark-meson scatterings counterbalance the momentum effects on the curvature, or the LPA' computation with a 3d regulator in [22] does not cover the full momentum dependence. The results for this investigation will be presented elsewhere.

IV. CONCLUSION

In the present work we have discussed the relation between different mesonic mass scales in low-energy QCD within a $N_f = 2$ quark-meson model. To that end we have computed fully momentum-dependent two-point functions of pions and the σ -meson as well as a full mesonic potential within a functional renormalisation group approach. This allows us to compare pole, screening and curvature masses both at vanishing and finite temperature; respective definitions are discussed in detail in Section II B. Whereas pole and screening mass coincide by definition for vanishing temperature they start to deviate at finite temperatures. Moreover, we find that the fluctuation scales for density fluctuations, related to the pole masses at vanishing temperature, and that for quantum and thermal fluctuations, related to the curvature masses, almost agree.

The present momentum-dependent set-up has also been used to evaluate the reliability of lower order approximations. In the present work we considered the two standard approximations to the QM model: the local potential approximation (LPA), where only classical propagators and the full mesonic potential are considered, and LPA', which additionally involves constant wavefunction renormalisations for the mesonic fields. Our results show a very good agreement between the fully momentum-dependent calculation and the LPA' calculation with relative deviations of at most 3% in a narrow region around the pseudo-critical temperature, which justifies the use of the LPA' as simple but very reliable truncation which includes already a large part of the momentum dependence of the full propagator.

In turn, we observe a large mismatch between the pion onset and curvature masses in LPA at vanishing temperature which reaches 38% for typical UV cutoff scales $\Lambda_{UV} = 700$ MeV, which has important implications for the relative fluctuation scales for vacuum/thermal and density fluctuations. Neglecting these effects leads to large systematic errors at finite chemical potential. Moreover, even at very low UV cutoff scales the LPA truncation for fixed initial conditions in the UV does not lead to quantitatively correct results compared to the outcome of the

full calculation.

In the line of these findings we estimated the effect of this mismatch of quantum/thermal versus density fluctuation scales in LPA within a simple rescaling the chemical potential axis accordingly, see Section III C. This simple argument leads to a result for the curvature of the chiral phase boundary, which lies reasonably close to the lattice result, but remains to be checked in larger truncation schemes.

An investigation of the combination of the approximation in [22] with $O(4)$ -symmetric regulators and full momentum dependence at finite density will be presented elsewhere. This requires the extension of the present 4d regulator classes to finite chemical potential, which is also tightly linked to the computation of real time quantities such as spectral functions in a fully $O(4)$ and Minkowski-invariant set-up, which will be discussed in a future publication. The present findings strongly emphasise the necessity of such a symmetry-preserving approach.

ACKNOWLEDGMENTS

We thank L. Fister, F. Rennecke and L. von Smekal for discussions. JMP thanks the Yukawa Institute for Theoretical Physics, Kyoto University. Discussions during the YITP workshop YITP-T-13-05 on 'New Frontiers in QCD' were useful to complete this work. This work is supported by the Helmholtz Alliance HA216/EMMI and the grant ERC-AdG-290623.

Appendix A: Truncation and flow equations

In this Appendix we discuss details on the truncation scheme as well as explicit expressions for the flow equations for the effective potential and the two-point function.

The flow equation for the momentum-dependent part of the two-point function involves the full three-point vertices, which in turn carry a non-trivial momentum dependence. At this point we completely neglect the momentum dependence of these vertices and simply determine them from the effective potential. Note in particular that the iteration procedure only involves the difference $\Delta\Gamma_k^{(2)}(p)$ between the two-point function evaluated at finite and at vanishing external momentum. Note fur-

thermore that the terms proportional to Y_k even in our expansion lead to momentum-dependent three- and four-point vertices. Taking into account these terms in the calculation will lead to a Λ^2 -rise instead of the correct Λ^{-2} -decay from the factorization property which is linked to the fact that the derivative expansion only works well for $p^2/k^2 \ll 1$. We want a procedure which is correct at vanishing and at asymptotically large momenta where in both cases the Y_k contribution to the three-point vertices is absent and is expected to be subleading also for intermediate momenta. Therefore, we determine the mesonic three-point vertices solely from the effective potential, for explicit expressions see [9, 42]. The full inverse two-point function $\Gamma^{(2)}$ is obtained via

$$\Gamma^{(2)}(p) = \Delta\Gamma^{(2)}(p) + U^{(2)}, \quad (\text{A1})$$

where $U^{(2)}$ denotes the appropriate second field derivative of the effective potential. As pointed out in Sec. II B, the momentum-dependent propagator now allows to calculate different particle masses. Thereby the calculation of screening, pole and onset masses requires analytical continuation, which is here performed by means of Chebyshev approximation. For the purpose of estimating the corresponding error, we have varied the Chebyshev approximation's order N_{cheb} over a range of $N_{\text{cheb}} \in \{50, \dots, 100\}$.

Next we specify the explicit expressions for the flow equations for the effective potential and the two-point function. Here, we employ 4d regulator functions of the form

$$R_k^{B/F}(q^2) = \Delta\Gamma_{B/F,k}^{(2)}(q^2, \rho_0) \cdot r(q^2/k^2). \quad (\text{A2a})$$

All practical calculations are performed using an exponential regulator shape function,

$$r(x) = x^{m-1}/(e^{x^m} - 1), \quad (\text{A2b})$$

with $m = 2$. The equation for the effective potential reads

$$\partial_t U_k = \frac{1}{2} I_{B,k}^{(1)}(m_\sigma^2) + \frac{N-1}{2} I_{B,k}^{(1)}(m_\pi^2) - 4N_c N_f I_{F,k}^{(1)}(m_\psi^2), \quad (\text{A3})$$

where $m_\pi^2 = 2U'$, $m_\sigma^2 = 2U' + 4U''\rho$ and $m_\psi^2 = h^2\rho$. The flow equations for the inverse pion and sigma meson two-point functions are given by [42]

$$\begin{aligned} \partial_t \Delta\Gamma_{\pi,k}^{(2)}(p^2, \rho) &= \rho (4U'')^2 \cdot \left(\Delta J_{B,k}(p^2; m_\sigma^2, m_\pi^2) + \Delta J_{B,k}(p^2; m_\pi^2, m_\sigma^2) \right) \\ &\quad - 8N_c N_f h^2 \cdot \left(\Delta J_{F,k}^{(1)}(p^2) - 2m_\psi^2 \Delta J_{F,k}^{(2)}(p^2) + m_\psi^2 \Delta J_{F,k}^{(3)}(p^2) \right), \end{aligned} \quad (\text{A4})$$

$$\begin{aligned} \partial_t \Delta\Gamma_{\sigma,k}^{(2)}(p^2, \rho) &= \rho (12U'' + 8\rho U''')^2 \cdot \Delta J_{B,k}(p^2; m_\sigma^2, m_\sigma^2) + (N-1) \rho (4U'')^2 \cdot \Delta J_{B,k}(p^2; m_\pi^2, m_\pi^2) \\ &\quad - 8N_c N_f h^2 \cdot \left(\Delta J_{F,k}^{(1)}(p^2) + 2m_\psi^2 \Delta J_{F,k}^{(2)}(p^2) + m_\psi^2 \Delta J_{F,k}^{(3)}(p^2) \right). \end{aligned} \quad (\text{A5})$$

Here, we have defined $\Delta J_k(p^2) = J_k(p^2) - J_k(0)$. Note that the first lines of the flow equations (A3)–(A5) can be identified with bosonic contributions, whereas the second lines constitute fermionic ones. Finally, the functions occurring on the right-hand sides of the above flow equations are given by

$$\begin{aligned} I_{\pi,k}^{(1)}(m^2) &= \oint_q \frac{\partial_t(\Delta\Gamma_{\pi,q}^{(2)} r_q)}{\Delta\Gamma_{\pi,q}^{(2)}(1+r_q) + m^2}, \\ I_{\sigma,k}^{(1)}(m^2, \rho) &= \oint_q \frac{\partial_t(\Delta\Gamma_{\sigma,q}^{(2)} r_q)}{\Delta\Gamma_{\sigma,q}^{(2)}(1+r_q) + m^2 + (\rho - \rho_0)Y_q q^2}, \\ I_{F,k}^{(1)}(m^2) &= \oint_q \frac{q^2 \dot{r}_q(1+r_q)}{q^2(1+r_q)^2 + m^2}. \end{aligned}$$

We employ the abbreviation $r_q \equiv r(q^2/k^2)$. Analogously, we have written Y_q instead of $Y_k(q^2)$ and similar for $\Delta\Gamma_q^{(2)}$. In addition, one finds

$$\begin{aligned} J_{B,k}(p^2; m_A^2, m_B^2) &= \oint_q \frac{\partial_t(\Delta\Gamma_{\pi,q}^{(2)} r_q)}{[\Delta\Gamma_q^{(2)}(1+r_q) + m^2]_A^2 [\Delta\Gamma_{p+q}^{(2)}(1+r_{q+p}) + m^2]_B}, \\ J_{F,k}^{(1)}(p^2; m^2) &= - \oint_q \frac{\dot{r}_q(1+r_q)^2(1+r_{p+q})q^2 q \cdot (q+p)}{(q^2(1+r_q)^2 + m^2)^2 ((q+p)^2(1+r_{q+p})^2 + m^2)}, \\ J_{F,k}^{(2)}(p^2; m^2) &= \oint_q \frac{\dot{r}_q(1+r_q)q^2}{(q^2(1+r_q)^2 + m^2)^2 ((q+p)^2(1+r_{q+p})^2 + m^2)}, \\ J_{F,k}^{(3)}(p^2; m^2) &= \oint_q \frac{\dot{r}_q(1+r_{p+q})q \cdot (q+p)}{(q^2(1+r_q)^2 + m^2)^2 ((q+p)^2(1+r_{q+p})^2 + m^2)}. \end{aligned}$$

The particle indices $A, B \in \{\pi, \sigma\}$ in the denominator affect both the inverse propagators and the mass terms.

Appendix B: Iteration procedure

The starting point is the calculation of the full effective potential using classical propagators which is then used as input for the calculation of the momentum-dependent part of two-point functions. Since the equation for the two-point function requires derivatives of the effective potential at field value ρ_0 as input, the flow equation for the effective potential is conveniently solved using a Taylor expansion at a fixed expansion point, see [22] for details. The calculation of the momentum-dependent propagators and their feedback then constitutes the first iteration step which is subsequently repeated until convergence is reached.

Most importantly, we want the expansion point in the final iteration step to coincide with the (IR-)minimum of the effective potential, as we restrict ourselves to the zeroth order in the field expansion of the two-point function. In every iteration step the expansion point is chosen such that it coincides with the minimum of the effective potential in that particular iteration step. Subsequently, the two-point function is then computed using the couplings at the same expansion point. This construction ensures that the expansion point converges towards the minimum of the effective potential in the converged re-

sult with a propagator evaluated at the same point. Furthermore only couplings at the minimum of the effective potential enter the calculation and one never expands inside the shallow region of the potential.

Appendix C: Thermal range

Usually the initial conditions are kept temperature-independent. This is only consistent for sufficiently large initial scales Λ_{UV} . For large cutoff scales they provide the characteristic mass scale of the (regularised) model. In thermal perturbation theory the thermal range is given by $\exp(-m/(2T))$, with m being the mass of the theory. Hence we expect that thermal fluctuations are suppressed exponentially with $\exp(-k/(\alpha_{\text{reg}}T))$ with a regulator-shape-function-dependent factor α_{reg} , see [33, 43, 44] for a discussion of thermal flows. In Sec. III A we have discussed the relation between cutoff scales for different regulators, see page 6, left column. Hence, without the shape dependence of α_{reg} the ratio of thermal ranges for different regulators should agree with that of the UV cutoff scales discussed in Sec. III A. Below we consider as in Sec. III A the 3d optimized regulator and the 4d exponential regulators with $m = 1, 2$. The comparison of the latter provides information about the shape dependence of α_{reg} .

For a given maximal temperature of interest T_{max} , we define a minimal UV cutoff scale $\Lambda_T^{(n)}$ by the condition that the UV flow of the coupling λ_n stays approximately temperature-independent above that scale, i.e.

$$\left| \frac{\dot{\lambda}_n^{T=T_{\text{max}}}(k) - \dot{\lambda}_n^{T=0}(k)}{\dot{\lambda}_n^{T=0}(k)} \right| < 0.05 \quad \text{for } k > \Lambda_T^{(n)}, \quad (\text{C1})$$

where the chosen bound of five percent on the right hand side is clearly strongly model-dependent. However, we emphasise that the criterion from above is conservative in the sense that the resulting deviation in the infrared will be significantly smaller than 5%. Here we consider the flows of the two relevant parameters λ_1 and λ_2 corresponding to mass and ϕ^4 -coupling. The cleanest set-up to investigate this question is that of single field mode flows where the corresponding dimensionless mass parameter $\omega = m^2/k^2$ is set to zero. This allows to compare the thermal range of different regulator functions.

regulator	$\Lambda_{T,\text{bos}}^{(1)}$	$\Lambda_{T,\text{bos}}^{(2)}$	$\Lambda_{T,\text{ferm}}^{(1)}$	$\Lambda_{T,\text{ferm}}^{(2)}$
4d exp. ($m = 1$)	3.8	4.6	3.1	3.1
4d exp. ($m = 2$)	5.5	4.8	6.75	6.75
3d Litim	5.6	6.9	5.6	6.9

TABLE VI. Thermal range from a single bosonic/fermionic field mode as defined by (C1) for different regulator functions. All ranges are given in units of the maximal temperature T_{max} . For $m = 2$ an exponential enveloping function was used.

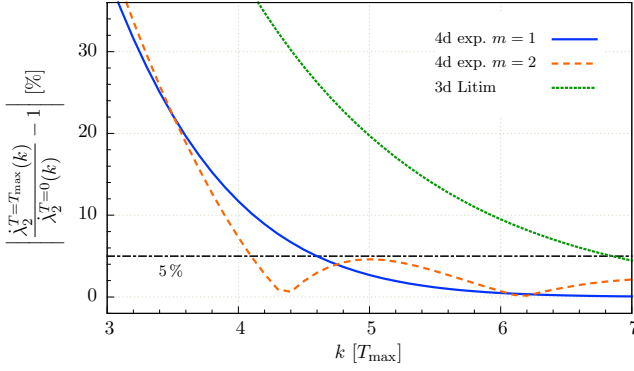


FIG. 7. Thermal range for a single bosonic field mode for different regulator functions.

Let us recall the (bosonic) cutoff ratios discussed in Sec. III A with $k_{3d}/k_{4d,m=1} \approx 3/2$ and $k_{3d}/k_{4d,m=1} \approx 5/4$ for the exponential regulators defined in (A2). For $m = 1$ this fits well to the ratio of thermal ranges $\Lambda_{T,bos,3d}/\Lambda_{T,bos,4d,m=1} \approx 3/2$. In turn, for $m = 2$ the ratios vary with large uncertainties, and are structurally smaller than the cutoff ratios. This comes from the sharp decay of the $m = 2$ cutoff function which increases the thermal range, see [43] for computations for the pressure.

Appendix D: Characteristic scales

Λ_{cl} is defined as the scale until which a description with a classical Lagrangian at the UV scale in the sense of a ϕ^4 -potential is sufficient in order to reach the full result in the IR. More concretely, starting from a given UV scale Λ_{UV} the full flow is integrated down to a lower scale $\Lambda'_{UV} < \Lambda_{UV}$ where a global rescaling is applied in order to achieve $Z_{\Lambda'_{UV}}(0) = 1$. The corresponding rescaled relevant couplings along with a classical propagator are used as input for a full calculation starting from Λ'_{UV} . We define Λ_{cl} as the scale above which the IR observables such as masses and the minimum of the effective potential do not deviate significantly from the result of the full calculation initiated at Λ_{UV} . The calculation for the determination of Λ_{cl} is illustrated in Fig. 8. Interestingly, in LPA the deviation never exceeds 0.2 %, which is consistent although not equivalent to the statement that the ϕ^4 truncation already leads to quantitatively correct results in LPA. Also in the full calculation the relative deviation never exceeds 3 % but peaks at 1.1 GeV and 0.3 GeV, where the dominant contributions from the fermionic/bosonic flow arise. In this sense the quark-meson model at vanishing temperature is trivial as it can be described quantitatively using a classical potential. This is a consequence of the fermionic contributions to the flow, whereas it no longer remains true upon increasing the number of bosons or reducing the number the number of fermions like in the purely bosonic $O(N)$ model, where also the convergence properties of the Tay-

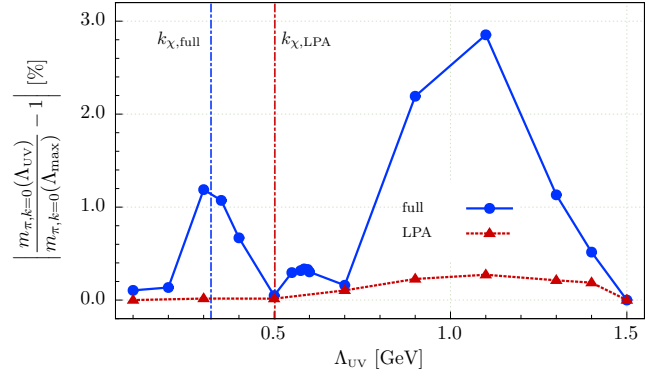


FIG. 8. Determination of Λ_{cl} for LPA and for the full calculation.

lor expansion worsen significantly. The same is true for the case of finite temperature where higher-order contributions are required to observe convergence in the Taylor expansion [22].

Finally, for a meaningful comparison between LPA and the full calculation, it is insightful to define the scale Λ_{LPA}^* which is the largest cutoff scale in which an LPA calculation with initial conditions from the full calculation shows chiral symmetry breaking. This puts a natural upper limit on possible UV cutoff scale for LPA calculations using QCD initial conditions. The determination of Λ_{LPA}^* is illustrated in Fig. 9, where we plot pion mass and minimum of the effective potential in the IR as a function of the UV cutoff scale Λ_{UV} , where a LPA calculation with initial conditions from the full calculation was initiated. Only below 600 MeV the LPA calculation shows chiral symmetry breaking, which is the largest scale for which a comparison to the full calculation using fixed UV initial conditions is possible. A more reasonable scale for this comparison which is used in this

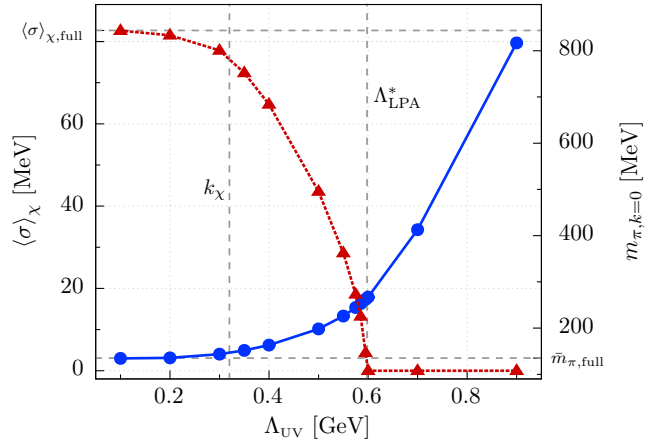


FIG. 9. Determination of the scale Λ_{LPA}^* : Pion mass and minimum of the effective potential in the IR as function of the UV cutoff scale Λ_{UV} , where a LPA calculation with initial conditions from the full calculation was initiated.

work is 500 MeV, where the chiral condensate in the LPA calculation reaches at least one half of the value from the full calculation. However, the cutoff scale can not be lowered to arbitrarily small scales, where the LPA result will converge towards the result of the full calculation by construction, as this just implies storing the full flow in the initial condition for the LPA calculation. In any case a lower bound for these fluctuation scales is provided by the the spontaneous symmetry breaking scale k_χ , which is found at $k_\chi \approx 320$ MeV in the full calculation.

Appendix E: Initial conditions

In this appendix, we specify the initial conditions used in the calculations presented in this paper. The UV potential is taken as

$$U_{k=\Lambda_{UV}} = a\phi^2 + b\phi^4 \quad (E1)$$

and the explicit symmetry breaking term is taken to be $-c\sigma$.

Λ_{UV} [GeV]	a/Λ_{UV}^2	b	c/Λ_{UV}^3	σ_0 [MeV]
0.5	0.608	2.446	0.0183	69.4
0.7	1.021	2.334	0.0083	55.5
0.9	1.304	2.055	0.0047	48.0
1.4	1.795	0.505	0.0018	34.0

TABLE VII. Initial conditions for full calculations with physical IR masses. The renormalised Yukawa coupling is $\bar{h} = 3.226$ for all UV cutoff scales.

Λ_{UV} [GeV]	a/Λ_{UV}^2	b	c/Λ_{UV}^3	σ_0 [MeV]
0.5	-0.009	5.812	0.0136	93.0
0.7	0.352	4.676	0.0049	93.0
0.9	0.532	3.451	0.0024	93.0
1.4	0.735	0.531	0.0006	93.0

TABLE VIII. Initial conditions for LPA calculations with physical IR masses. The Yukawa coupling is $h = 3.226$ for all UV cutoff scales.

Appendix F: Convergence properties

In this appendix, we investigate the iteration procedure's convergence properties by comparing a given observable obtained from different iteration steps. Exemplarily, we choose this observable to be the chiral condensate. Accordingly, Fig. 10 shows the relative deviation between the chiral condensate $\langle\sigma\rangle$ in step i and the converged result $\langle\sigma\rangle_{\text{conv}}$. We restrict ourselves to an analysis of the convergence properties at vanishing temperature. However, in the finite temperature case the

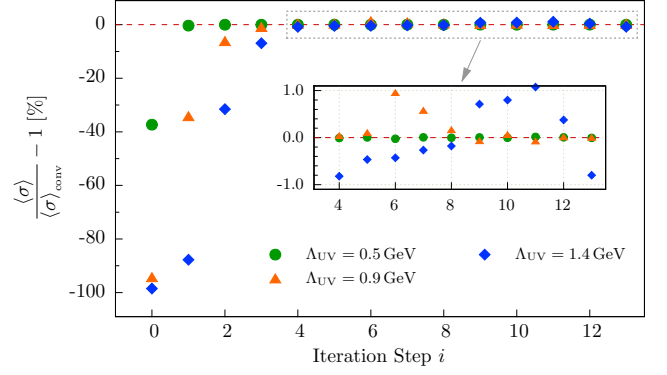


FIG. 10. Convergence of the iteration procedure for different UV cutoff scales.

iteration procedure requires at most one additional iteration step to converge. As pointed out in the main text keeping the bare or the renormalised Yukawa coupling constant has crucial impact on the convergence properties of the iteration procedure. As shown in Tab. IX in comparison to Tab. III in the main text, the iteration for constant bare Yukawa coupling converges significantly faster than the corresponding calculation with constant renormalised Yukawa coupling at the same cutoff scale. Disregarding the fact that a constant bare Yukawa coupling does not correspond to the physical situation, it is not even possible in this case to find initial conditions for $\Lambda_{UV} > 700$ MeV which lead to physical parameters in the IR due to the stronger running of the wavefunction renormalisation compared to the calculation with fixed renormalised Yukawa coupling.

The dependence of the convergence properties on the UV cutoff scale are illustrated in Fig. 10. If one considers relative deviations of one percent from the full result as approximately converged the calculation at $\Lambda_{UV} = 500$ MeV and $\Lambda_{UV} = 900$ MeV converge after the first or third iteration step respectively, whereas the calculation at $\Lambda_{UV} = 1.4$ GeV requires four iteration steps to converge.

step	m_{cur} [MeV]	m_{pol} [MeV]	σ_{min} [MeV]
0	202.5	202.5	93.0
1	135.6	134 ± 2	140.8
2	135.5	135 ± 2	140.8
5	135.5	135 ± 2	140.8

TABLE IX. Similar to Tab. III for $\Lambda = 900$ MeV but for a fixed bare Yukawa coupling.

Appendix G: Comparison LPA' versus full calculation

In order to understand why Figs. 4 and 5 show only little deviations between the LPA' result and the full cal-

culation with momentum-dependent meson propagators, we reinvestigate the corresponding truncations, putting emphasis on the role of the regulator function within the FRG framework. For the sake of simplicity, let us thereby start with the situation at vanishing temperature, where the two-point correlator's momentum-dependent part can be written as

$$\Delta\Gamma_k^{(2)}(p^2) = Z_k(p^2)p^2 \equiv (1 + \delta Z_k(p^2))p^2 \quad (\text{G1})$$

due to Euclidean $O(4)$ symmetry. For future reference, we define the quantity δZ via the second equality in (G1), which isolates the non-quadratic and hence non-trivial dependence of the bosonic two-point functions on the external momentum. Next, recall that one central aspect of the Wilsonian renormalisation group is the locality of RG flows in momentum space, which is realised in the FRG via an appropriately chosen regulator function R_k . From a technical point of view, the calculation of loop integrals therefore effectively involves only loop momenta p_μ from within a thin momentum shell around the current RG scale, i.e. $p^2 \approx k^2$, as large momentum modes are regularised by the cutoff insertion $\partial_t R_k$, while fluctuations with smaller momenta are suppressed by the additional regulator term in the exact two-point correlator, $\Gamma_k^{(2)} + R_k$. Consequently, not the full momentum dependence of the propagators is resolved in computing RG flows at a given scale k , anyway.

In conclusion, the absence of fully momentum-dependent correlation functions can be partly compensated for in FRG calculations by choosing a proper regulator function. Thus, a momentum-independent but RG scale-dependent wavefunction renormalisation Z_k can be a reasonable approximation for the full $Z_k(p^2)$.

The above reasoning can be explicitly verified by studying the numerically obtained propagators from both LPA' and the full calculation. In Fig. 11, we therefore compare the non-trivial momentum dependencies in the aforementioned models. In view of the previous discussion, we have normalised external momenta $p = \sqrt{p^2}$ to

the given RG scale k . Indeed, one immediately recognises that the correlators nearly coincide for all $p^2 \lesssim k^2$. Thus, the plot explicitly demonstrates that some of the propagator's full momentum dependence is effectively taken into account even by a momentum-independent approximation such as LPA'. Furthermore, deviations between the two truncations continue to be relatively small in the regime $p/k \in [1, 2]$.

Besides, practical calculations do not involve $\delta Z \cdot p^2$ alone, but rather $Z \cdot p^2$, the dominant behaviour of which is usually given by the term quadratic in p^2 , such that the aforementioned differences will have even less impact on the outcome. Especially interesting is furthermore the combination $G\dot{R}G$ appearing e.g. in the flow equation of $\partial_\rho U_k$, which, in turn, is the quantity relevant to calculate the chiral condensate or the pion curvature mass. We show $(G\dot{R}G)_k(p^2)$ as obtained in the different truncations in the inlay plot of Fig. 11.

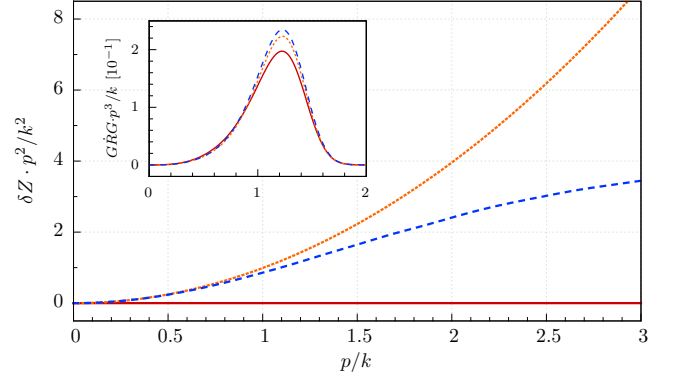


FIG. 11. Momentum dependence of the inverse pion propagator. We compare both $\delta Z \cdot p^2$ and $G\dot{R}G \cdot p^3$ for the full truncation (dashed, blue line), LPA' (dotted, orange line) and LPA (solid, red line). Exemplarily, we show the case $k = 400$ MeV and $\Lambda_{UV} = 700$ MeV, where the full calculation has a physical IR.

-
- [1] J. Braun, L. M. Haas, F. Marhauser, and J. M. Pawłowski, Phys.Rev.Lett. **106**, 022002 (2011), 0908.0008.
 - [2] J. M. Pawłowski, AIP Conf.Proc. **1343**, 75 (2011), 1012.5075.
 - [3] L. M. Haas, R. Stiele, J. Braun, J. M. Pawłowski, and J. Schaffner-Bielich, Phys.Rev. **D87**, 076004 (2013), 1302.1993.
 - [4] T. K. Herbst, M. Mitter, J. M. Pawłowski, B.-J. Schaefer, and R. Stiele, Phys.Lett. **B731**, 248 (2014), 1308.3621.
 - [5] N. Strodthoff, B.-J. Schaefer, and L. von Smekal, Phys.Rev. **D85**, 074007 (2012), 1112.5401.
 - [6] K. Kamikado, N. Strodthoff, L. von Smekal, and J. Wambach, Phys.Lett. **B718**, 1044 (2013), 1207.0400.
 - [7] E. E. Svanes and J. O. Andersen, Nucl.Phys. **A857**, 16 (2011), 1009.0430.
 - [8] S. Floerchinger, JHEP **1205**, 021 (2012), 1112.4374.
 - [9] R.-A. Tripolt, N. Strodthoff, L. von Smekal, and J. Wambach, Phys.Rev. **D89**, 034010 (2014), 1311.0630.
 - [10] R.-A. Tripolt, L. von Smekal, and J. Wambach, (2014), 1408.3512.
 - [11] U. Ellwanger and C. Wetterich, Nucl.Phys. **B423**, 137 (1994), hep-ph/9402221.
 - [12] D. Jungnickel and C. Wetterich, Phys.Rev. **D53**, 5142 (1996), hep-ph/9505267.
 - [13] J. Berges, D. Jungnickel, and C. Wetterich, Phys.Rev. **D59**, 034010 (1999), hep-ph/9705474.
 - [14] B.-J. Schaefer and J. Wambach, Nucl.Phys. **A757**, 479 (2005), nucl-th/0403039.
 - [15] H. Gies and C. Wetterich, Phys.Rev. **D65**, 065001 (2002), hep-th/0107221.
 - [16] H. Gies and C. Wetterich, Phys.Rev. **D69**, 025001

- (2004), hep-th/0209183.
- [17] J. M. Pawłowski, *Annals Phys.* **322**, 2831 (2007), hep-th/0512261.
 - [18] S. Floerchinger and C. Wetterich, *Phys.Lett.* **B680**, 371 (2009), 0905.0915.
 - [19] C. S. Fischer, A. Maas, and J. M. Pawłowski, *Annals Phys.* **324**, 2408 (2009), 0810.1987.
 - [20] C. Wetterich, *Z.Phys.* **C57**, 451 (1993).
 - [21] J. Berges, N. Tetradis, and C. Wetterich, *Phys. Rept.* **363**, 223 (2002), hep-ph/0005122.
 - [22] J. M. Pawłowski and F. Rennecke, (2014), 1403.1179.
 - [23] J. Braun, *Phys.Rev.* **D81**, 016008 (2010), 0908.1543.
 - [24] T. D. Cohen, *Phys.Rev.Lett.* **91**, 222001 (2003), hep-ph/0307089.
 - [25] H. Gies, *Lect.Notes Phys.* **852**, 287 (2012), hep-ph/0611146.
 - [26] B.-J. Schaefer and J. Wambach, *Phys.Part.Nucl.* **39**, 1025 (2008), hep-ph/0611191.
 - [27] J. Braun, *J.Phys.* **G39**, 033001 (2012), 1108.4449.
 - [28] C. Wetterich, *Phys.Lett.* **B301**, 90 (1993).
 - [29] U. Ellwanger, M. Hirsch, and A. Weber, *Z.Phys.* **C69**, 687 (1996), hep-th/9506019.
 - [30] B. Bergerhoff and C. Wetterich, *Phys.Rev.* **D57**, 1591 (1998), hep-ph/9708425.
 - [31] J. M. Pawłowski, D. F. Litim, S. Nedelko, and L. von Smekal, *Phys.Rev.Lett.* **93**, 152002 (2004), hep-th/0312324.
 - [32] J.-P. Blaizot, R. Mendez-Galain, and N. Wschebor, *Phys.Rev.* **E74**, 051116 (2006), hep-th/0512317.
 - [33] L. Fister and J. M. Pawłowski, (2011), 1112.5440.
 - [34] L. Canet, B. Delamotte, D. Mouhanna, and J. Vidal, *Phys.Rev.* **B68**, 064421 (2003), hep-th/0302227.
 - [35] D. F. Litim and D. Zappala, *Phys.Rev.* **D83**, 085009 (2011), 1009.1948.
 - [36] M. Mitter, J. M. Pawłowski, and N. Strodthoff, (in prep.).
 - [37] W. Florkowski and B. L. Friman, *Acta Phys.Polon.* **B25**, 49 (1994).
 - [38] F. Marhauser and J. M. Pawłowski, (2008), 0812.1144.
 - [39] F. Benitez *et al.*, *Phys.Rev.* **E85**, 026707 (2012), 1110.2665.
 - [40] I. Boettcher, J. M. Pawłowski, and C. Wetterich, *Phys.Rev.* **A89**, 053630 (2014), 1312.0505.
 - [41] P. de Forcrand and O. Philipsen, *Nucl.Phys.* **B642**, 290 (2002), hep-lat/0205016.
 - [42] K. Kamikado, N. Strodthoff, L. von Smekal, and J. Wambach, *Eur.Phys.J.* **C74**, 2806 (2014), 1302.6199.
 - [43] L. Fister, *On the Phase Diagram of QCD with Dynamical Quarks*, PhD thesis, Universität Heidelberg, 2012.
 - [44] D. F. Litim and J. M. Pawłowski, *JHEP* **0611**, 026 (2006), hep-th/0609122.